

Influence of iron doping on the photocatalytic activity of nanocrystalline TiO₂ particles fabricated by ultrasound method for enhanced degradation of organic dye

Mohamed Saber Lassoued,^{a, b, c*} Abdelmajid Lassoued,^a Mohammed. S. M. Abdelbaky,^c
Salah Ammar,^a Abdellatif Gadri,^a Abdelhamid Ben Salah,^b and Santiago García-Granda^c

^a *Unité de recherche Electrochimie, Matériaux et environnement UREME (UR17ES45),
Faculté des Sciences de Gabès, Université de Gabès, Cité Erriadh, 6072 Gabès, Tunisie*

^b *Material and Environment Science Laboratory, Science Faculty of Sfax University, P.B
1171,3000 Sfax, Tunisia*

^c *Department of physical and analytical chemistry, Oviedo University-CINN,33006 Oviedo,
Spain*

Corresponding author e-mail address: lassoued_saber@yahoo.com

Abstract

Synthesis and characterization of Fe doped TiO₂ composite with iron concentration varying from 0 to 7% as a photocatalyst in the photodegradation of methylene orange on UV/visible light irradiation in a closed reactor has been carried out. Synthesis was conducted by the ultrasound method at room temperature using Tetrabutyl titanate and Iron (III) Chloride 6-hydrate as a precursor, followed by thermal treatment at a temperature of 600 °C. The characterizations were performed using X-ray diffraction (XRD), transmission electron microscopy (TEM), scanning electron microscopy (SEM), FT-IR spectrometry, thermal analysis, UV-Vis diffuse reflectance spectrophotometer, Photoluminescence and Brunauer-Emmett-Teller (BET). XRD spectra revealed that samples crystallized in the anatase phase at 600 °C. The transmission and scanning electron microscopy were used to detect the morphology of synthesized nanoparticles, which sizes changed with the altitude in the doping

concentration to 7%. FTIR spectra exhibit broad peaks where anatase phases of TiO₂ demonstrate very sharp peaks. In accordance with UV–visible absorption measurements, this diminution of nanoparticles sizes was followed by a decrease in the band gap value from 3.21 eV, for undoped TiO₂, to 2.46 eV, for TiO₂ doped at 7%. The TGA showed three mass losses, whereas DTA resulted in three endothermic peaks. The maximum photoconversion efficiency was 2.5%, which was 6 times the photoconversion efficiency of undoped TiO₂. Finally, the prepared materials were used to photocatalyse the decolourization of methylene orange (MO) in aqueous medium as a model compound under the illumination of visible light ($\lambda = 420$ nm).

Keywords:

Oxide titanium; Iron doped; X-ray; TEM; UV–visible and photocatalytic activity.

Introduction

Over the last few decades, much consideration has been given to a number of nanostructured metal oxide semiconductors which have been studied owing to their interesting physical properties including non-linear optical activity, photoluminescence and electrical properties [1-6] and their potential applications in various fields, such as photocatalysis to decompose undesirable organic matters [7-9], optical coating, solar cells [10, 11], filters for catalyst supports [12] but also white pigment for paints or cosmetics [13], which could well lead to technological innovation.

Among these sought-after materials, titanium oxides, as anatase-type TiO₂ have received considerable attention as functional materials due to its strong oxidizing power, non-toxicity, low cost, and long-term photostability [14-19]. The photocatalytic performance was improved through the use of TiO₂ nanoparticles [20-23] or the use of supported TiO₂ [24], both achievements enhanced the photodegradation rates in comparison with neat titania. However, TiO₂ nanostructures suffer from some limitations, due to its large band gap which is around

3.2 eV and low electron transfer rate which impedes its application. So, it has been reported that doping TiO₂ with metal ions may enhance its photoactivity [25-27] or even may enable its sensitization under visible light [28].

Among all the metal ions used for TiO₂ doping, Iron ion has been proven to be helpful dopants for extending the photo response of TiO₂ through reducing its band gap and introduce visible photoresponse [29, 30] thanks to the fact that the ionic radii of Ti⁴⁺ (0.605 Å) and Fe³⁺ (0.680 Å) are roughly similar, which favors the substitution of Ti⁴⁺ by Fe³⁺ in the TiO₂ crystal lattice to form a stable solid solution [31].

Furthermore, several methods were used to prepare Fe doped TiO₂ such as sol-gel method [32, 33], hydrothermal [34] and mechanical alloying [35]. Among the methods reported in the literature, the ultrasound method is well-adapted to the fabrication of nanostructured materials because of its capacity to control the grain size.

In the present work, Fe doped TiO₂ aggregates made of TiO₂ nanoparticles as building units have been successfully prepared by ultrasound method and their characterization by XRD, TEM, SEM, FTIR, thermal analysis, UV absorption spectroscopy, photoelectrochemical measurements, Photoluminescence and BET. It has been shown that the increasing of added Fe dopant increases the size of TiO₂ nanoparticles building unit of prepared aggregates and reduces significantly its band gap energy at certain Fe dopant amount threshold. Finally, the photocatalytic properties of the materials prepared were investigated in the case of the photodegradation of MO under UV-light illumination, the greatest activity being found for the 7 at. % Fe-doped TiO₂ nanomaterial.

2 Experimental methods

2.1. Synthesis of Fe-TiO₂ nanoparticles

Undoped and Fe-doped Oxide Titanium powders were prepared by Ultrasound technique.

Ultrasound assisted synthesis of Fe doped TiO₂ was carried out as follows. Firstly, to prepare TiO₂ sol, 5 mL Tetrabutyl titanate [Ti (OC₄H₉)₄] was mixed with 50 mL absolute ethanol (46.07 M) and 0.33 mL H₂SO₄, (98%), followed by the addition of 250 mL deionized water and continuously stirred. Then, different amounts of Iron (III) Chloride 6-hydrate powder under stirring for 30 minutes dissolved in the TiO₂ sol and sonicated for 10 minutes (Ultrasonic processor, SONOREX SUPER RK 106, 35 kHz). After sonicated, the mixture was kept in a water bath at 80 °C for 2 h. Finally, the mixture was cooled to room temperature and washed with deionized water. All the as-synthesized products were almost amorphous phase and calcined at 600 °C for 1 hour.

A series of Fe-doped TiO₂ nanoparticles were prepared by changing the Fe/TiO₂ ratio from 1 to 7.0 mol%. In addition, an undoped TiO₂ nanoparticle was also prepared by the same procedure without the addition of Fe (**Fig. 1**).

2. 2. Investigation techniques

The characterization of the prepared compound was performed using X-ray diffraction, Transmission electron microscopy (TEM), Scanning electron microscopy (SEM), Infrared spectroscopy (IR), UV-visible analysis (UV), thermal analyses (TGA and DTA), photoelectrochemical measurements, Photoluminescence (PL) and Brunauer-Emmett-Teller (BET).

2 .3. Characterization

2 .3.1. XRD characterizations

The X-ray diffraction patterns of the samples were identified using German Bruker D2 PHASER X-ray diffractometer with CuK_α radiation (1.5418 Å) as a source. The intensity data were collected over the range of 20°–80° using a step scan mode (0.001°/s).

2.3.2. SEM, TEM and EDX measurements

Transmission Electron Microscopy (TEM) measurements were obtained on a JEOL 2011 transmission electron microscope with an accelerating voltage of 200 kV. The Scanning Electron Microscope (SEM) was collected on a scanning electron microscopy (SEM) type KYKY-EM3200, 25KV. Micro structural characteristics such as morphology Energy-dispersive X-ray analysis (EDX, voltage 20KV, Takeoff Angle 35.0°) was also used for the chemical analysis of the nano-particles.

2.3.3. Spectroscopy measurements

Fourier Transform Infra-Red (FT-IR) spectra of samples were explored by a NICOLET IR200 FT-IR spectrometer with transmission from 4000 to 400 cm^{-1} . The Ultraviolet-Visible (UV-Vis) absorption of the samples was recorded on SHIMADZU (UV-3101 PC) UV-Vis Spectrophotometer. Excitation and emission spectra of the samples were recorded by photoluminescence spectrophotometer (Avantes , Avaspec-2048-TEC) using a Xenon lamp as excitation source operating at 240 nm.

2.3.4. Flat band potential measurement and Photoelectrochemical measurements

The electron energy states of quasi-Fermi levels (${}_nE_F^*$) of Fe-doped TiO_2 (with 1, 3, 5, and 7 wt.% Fe) powders were measured using methylviologen dichloride (MV^{2+} , $E_{\text{red}} = -0.445$ V vs. normal hydrogen electrode, NHE) as a pH-independent redox system. The estimated pH_0 values were converted to the Fermi potentials (i.e., flat band potentials) at pH=7 by the equation ${}^*E_{F(\text{pH}=7)} = -0.445 + 0.059 \cdot (\text{pH}_0 - 7)$. Reproducibility of the pH values was better than 0.1 pH units. In a typical experiment, 30 mg of catalyst powder and 6 mg of MV^{2+} were suspended in a specially designed glass reactor cell having a flat quartz window (~75 mL of 0.1 M KNO_3). A platinum flag of 1 cm area and Ag/AgCl were served as working and reference electrodes, respectively, and a pH meter was used for recording the proton concentration. Prior to measurements, the solutions were purged with argon gas (>200

mL/min) for >2 h and continued the same during voltage measurements. Initially, the pH of the solution was adjusted to pH=1–2 prior to recording the voltage readings using a solution of HNO₃ (0.1 M). The light source was a Xenon arc lamp of 500 W (Solar Simulator, Oriel 91160) having AM 1.5G filter and a monochromator (Newport74125 model) with a bandwidth of 5 nm.

The photoelectrochemical measurements were carried out in a 3-electrode system with Ag/AgCl as a reference electrode, Pt wire as counter electrode, and the TiO₂ photoanode as the working electrode. The light source used was an Hg–Xe lamp (Newport, 500W) coupled with a AM1.5G filter, calibrated to 100 mW/cm² (1 sun illumination) with silicon diode. The electrolyte used for PEC measurement was 1 M KOH.

2.3.5. Thermal analysis

The thermal behavior was evaluated by Thermo Gravimetric (TGA) and Differential Thermal Analysis (DTA) in the air using TGA Q500 TA instrument.

2.3.6. BET

Specific surface areas (Brunauer-Emmett-Teller (BET)) of TiO₂ nanoparticles were deduced from N₂ sorption analyzes performed with Micromeritics ASAP2010 equipment.

2.4. Photocatalytic activity measurements

The photocatalytic activities of the Fe-doped TiO₂ nanoparticles (without catalyst, 1 mol%, 3 mol%, 5 mol % and 7 mol%) were analyzed based on the photodegradation of MO at room temperature. The solution was irradiated with UV (2 lamp, each power 15 W, wavelength 254 nm) and visible light (250W mercury lamp) under magnetic stirring, separately. In a typical photocatalytic experiment, 0.1 g of the sample was dispersed in 100 mL of MO aqueous solution. Before applying the irradiation, the suspension was magnetically stirred for 30 min in the dark to ensure that an adsorption–desorption equilibrium was reached between the Fe-doped TiO₂ nanoparticles and the aqueous dye solution. Samples of the solution were then

collected from the reactor at regular intervals, before centrifuging and analyzing to determine the residual amounts of the dye after photo-irradiation using a UV-Vis spectrophotometer (Shimadzu UV-2450).

3. Results and discussion

3.1 XRD Powder

The crystalline phase and structure of prepared powder at different Fe doping contents (wt 0 %, wt 1 %, wt 3 %, wt 5% and wt7%), were investigated by X-ray diffraction method. The obtained XRD patterns for some temperatures are presented in **Fig. 2(a)**, and it has revealed a crystalline structure with all the peaks assigned to TiO₂ anatase phase (JCPDS No. 89-4921) or TiO₂, which is a signature of material with high purity. These results are in good accordance with the findings of L. Wen et al. [36]. No characteristic peaks attributed to iron were detected, implying that Fe was successfully incorporated into the crystal lattice of anatase TiO₂ or the vanadium oxide was so small in content that it cannot be detected by a XRD technique [37]. In addition, the average crystallite sizes were calculated using Scherer analysis of the full width at half-maximum of the intense peak corresponding to (101) crystallographic plane [38]. The results are summarized in **Table 1**. It is observed that the crystallite size of Fe-doped TiO₂ nanoparticles decreases from 18 to 12 nm with the increase of doping concentration.

A closer analysis of XRD patterns of **Fig. 2(b)** and particularly the peaks corresponding to the crystallographic plane (101) TiO₂ shows a slight shift to a larger angle when the Fe doping content increases. This could be attributed to the substitution of Ti⁴⁺ by Fe³⁺ in the TiO₂ crystal lattice, and the fact that the ionic radii of Ti⁴⁺ (0.605 Å) is slightly smaller than that of Fe³⁺ (0.680 Å), which induces a formation of more compact crystal structure and a decrease of the corresponding lattice parameters [39]. As a result the lattice parameter 'c' values are

found to increase with Fe-doping concentration (**Fig. 3a**), however, The lattice parameter ‘a’ values are found relatively unchanged (**Fig. 3b**). It is obvious that the inclusion of Fe species in the lattice does not affect its lattice parameter ‘a’.

Where the lattice parameters ‘a’ and ‘c’ has been determined by the following expression [40], where d is the interreticular distance, a and c are the lattice constants and h, k, l are the Miller indices.

$$d_{hkl} = \frac{1}{\sqrt{\frac{h^2+k^2}{a^2} + \frac{l^2}{c^2}}} \quad (1)$$

‘d’ is the interreticular distance, ‘a’ and ‘c’ are the lattice constants and ‘h, k, l’ are the Miller indices.

From XRD data and by using the sheerer formula,

$$D = 0.9\lambda / \beta \cos\theta \quad (2)$$

Where $k = 0.94$, $\lambda = 1.54060\text{\AA}$, β = Full Width Half Maximum (FWHM) and θ = Diffracting angle, the crystallite size was calculated as shown in **Table 2**. From the results, it can be concluded that the crystallite size decreased by increasing of the iron dopant levels.

3.2 Particles size and morphology measurements: (TEM/SEM)

Size and morphology of the nanoparticles are determined by analyzing the recorded TEM images. **Fig. (4(a)–(e))** highlights the transmission electron microscope (TEM) images of the samples. The samples are made up of uniform nanoparticles of spherical morphology with narrow size distribution. The nanoparticles size depends largely on different iron doped titanium dioxide nanoparticles concentration (0 mol %, 1 mol %, 3 mol %, 5 mol % and 7 mol %). used in the synthesis of our compound. In the fact, the addition of Fe^{3+} ions (**Fig. 4(b-e)**) slightly increased the particle sizes of TiO_2 .

The surface of the nanocrystals is perceived and their sizes are determined by means of scanning electron microscopy (SEM). Microscopic observations of our samples show that

crystallites of pure and Fe-doped TiO₂ exhibited fine, spherical shape and nanometric size for the different synthesized samples (Fig. 5(a)–(e)). Sizes of nanoparticles depend on the concentration of copper (dopant) used in the synthesis of samples: the size of nanoparticles of TiO₂ decreases when the concentration of iron is increased; we go from 15 (±2) nm for pure TiO₂ up to 10 (±2) nm for 7% Fe-doped TiO₂.

The estimated values, obtained using TEM photograph, are in good argument with those obtained from the XRD data. It is noteworthy to mention that, similar to the results estimated using Scherer Method, the grain size estimated from TEM data (**Table 3**).

In order to establish the achievement of the targeted chemical composition in the synthesized powders, the 7.0 wt. % Fe-doped TiO₂ nano-particles was examined by EDX. **Fig.5 (f)** shows the presence of titanium and iron in the nano-particles. No impurities and reaction products were observed in the samples.

3 .3. FT-IR spectroscopic studies

FT-IR spectroscopy was used to detect the presence of functional groups absorbed on the surface of synthesized particles during precipitation process. **Fig. 6** presents the FT-IR spectra of Fe-TiO₂ (7mol %) and undoped TiO₂.

The uncalcined sample showed pics at 3300 attributed to vibrations (O–H) and pics observed at 1635 cm⁻¹ can be assigned to deformation (O–H) due to water molecules. Notably, the peaks at 453 cm⁻¹ are the contributions from the anatase titania.

Investigations FT-IR spectrum of Fe –doped TiO₂ nanoparticles calcined at 600 ° C show the absence of all bands related to the hydroxyl group OH. Yet, all organic species were removed after calcination. Then we noticed the appearance of two bands at 522 cm⁻¹ and 438 cm⁻¹ that can be attributed to the Fe-O-Ti vibration.

3.4. Thermal analysis (TGA and DTA)

The findings associated with formation and decomposition phase occurring during heat treatment of synthesized sample oxide titanium is in good agreement with Thermo Gravimetric Analysis and Differential Thermal Analysis (TGA and DTA) results. Thermal analysis was realized from room temperature to 500°C.

For TiO₂ nanoparticles, there are three distinct mass loss steps in the temperature ranges (**Fig. 7**). The first weight loss, step occurred gradually between [84°C – 122°C]. The mass loss was of 5.56%, and this loss of weight is attributed to the removal of water existing on the surface of TiO₂. Using DTA enabled us to find one endothermic peak at 109.92°C, The second step corresponds to a mass loss of 3.04% occurring at [182°C - 320°C], which is due to the combustible organic products present in our prepared sample. Through the use of DTA we recorded one endothermic peak at 210.28°C. The third step stands for a minor weight loss (1.38%) occurring in the range of [340°C - 560°C], which is due to the transition phase of synthesized compounds. Finally, using DTA helped us find one endothermic peak at 390.02°C. After 400°C, the curve becomes parallel to the temperature axis, which emphasizes high stability of TiO₂ nanoparticles. There is no associated signal with the thermal processes of TiO₂ nanoparticles in the TGA curve confirming the crystallization and phase transition of TiO₂ nanoparticles associated with them.

3.5. UV-Visible Analysis

The absorption spectra in the UV-Vis range of TiO₂: Fe nanoparticles with different Fe concentrations show that all absorption curves exhibit an intense absorption in the range of 200–800 nm wavelengths.

Although a quantum upon doping, a small decrease of the absorption edge is observed corresponding to a red-shift similar to the one observed in Mn doped TiO₂ and Cu doped

TiO₂ band gap (E_g [41, 42].) for Fe-doped oxide titanium nanoparticles can be determined by extrapolation from the absorption edge which is given by the following equation [43]:

$$(\alpha h\nu)^n = A (h\nu - E_g) \quad (4)$$

Where α is the absorption coefficient, A is a constant, $h\nu$ is the energy of light and n is a constant depending on the nature of the electron transition [44]. **Fig. 8a** shows the plot of $(\alpha h\nu)^{1/2}$ versus $h\nu$ from the intercept of the linear absorption edge part with the energy axis. When $(\alpha h\nu)^{1/2}$ is zero, the photon energy is E_g. Fe doped TiO₂ powders showed an optical band gap decrease from 3.21 to 2.47 eV when the copper concentration increased up to 7% (**Fig.8b**).

The flat band potential value was determined by measuring the photovoltages of Fe doped TiO₂ powders as a function of the suspension PH value (Fig. 9). The various parameters like Energy gap, Energy level of conduction band and valence band are classified in **Table 3**.

However, an increase in Fe-dopant concentration has caused an increasing trend in the flat band potentials (E_F). These values increased from -0.082 V for the 1 wt.% Fe-doped TiO₂ to -0.029 V for the 7 wt.% Fe doped TiO₂ (**Table 4**). This change in the flat band potential could be attributed to the various modifications such as, change in the crystallite size and specific surface area, the formation of certain additional secondary phases, etc., occurred to the TiO₂ powders upon doping with Fe.

3. 6. Photoconversion

The photoconversion efficiency η of light energy to chemical energy with an external applied potential E_{app} is calculated as

$$\eta(\%) = [(total\ power\ output - electrical\ power\ output) / light\ power\ input] * 100\%$$

$$= J_p [(E_{rev}^\circ - |E_{app}|) / I_0] * 100\%$$

where ' J_p ' is the photocurrent density (mA/cm), ' I_0 ' is the power density of incident light (mA/cm²). ' E_{rev}° ' is the standard state-reversible potential, and ' E_{app} ' is the applied

potential. A plot of photoconversion efficiency vs. applied potential is shown in Fig. 10. The optimal photo conversion efficiency can be up to 2.5% for 7 at.% Fe–TiO₂, while 0 at.% Fe–TiO₂, 1 at.% Fe–TiO₂, 3 at.% Fe–TiO₂ and 5 at.% Fe–TiO₂ can only achieve a photoconversion efficiency of 0.4 %, 0.7%, 1.4% and 1.9% respectively .

3.7. Photoluminescence

The PL spectroscopy has been broadly used to study the transition function of the photogenerated carriers in the semiconductors. PL emission spectra have been widely used to investigate the efficiency of charge carrier trapping and migration, and to understand the fact of electron-hole pairs in semiconductors. The measured PL, emission spectra are illustrated in **fig. 11**. It exhibits a strong peak at 390 nm, these emission bands originated from charge recombination at the shallow-trap surface state. This surface state originated from the oxygen vacancies which act as radiative centers [45]. The intensity of the PL spectra decreased for 7 wt% Fe- TiO₂. This result indicates that the PL-intensity reduction represents the decrease of the photogenerated pairs, recombination process. Broadly speaking, the lower the PL intensity demonstrates the lower recombination rate of the photogenerated electron-hole pairs, which leads to the higher photocatalytic activity [46].

3.8. Textural properties

Figure 12 (a, b) shows N₂ adsorption–desorption isotherms for pure TiO₂ and 7 at. % Fe–TiO₂ samples. As shown the inset of Fig. 12, and on the basis of IUPAC classification, each material showed a type II isotherm which is characteristic of materials including large mesopores and/or macropores [47].

The corresponding specific surface areas of the samples were calculated to be 5.54 m² g⁻¹ for pure TiO₂ and 30.64m²g⁻¹ for 7 at.% Fe–TiO₂. We find that the addition of either the [Fe] increased the specific surface area of the composite. The increase in the BET specific surface area suggests that this composite may exhibit improved photocatalytic degradation.

4. Photocatalytic activity

The capability of undoped TiO₂ and Fe-TiO₂ (1 mol %, 3 mol %, 5 mol % and 7 mol %) to degrade dye was evaluated through its application for degradation of methylene orange under visible light irradiation are shown in **Fig. 13**.

The percentage of degradation of MO dye was calculated from the following equation:

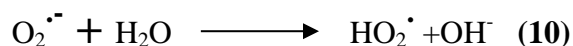
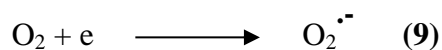
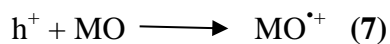
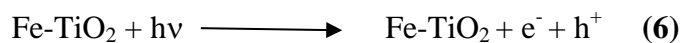
$$\text{Percentage of degradation} = (1 - C_t/C_0) * 100 \quad (5)$$

Where C₀ and C in **Fig. 13a** represent the initial concentration after the adsorption–desorption equilibrium for 30 min and the real-time concentration of MO, respectively.

Blank experiments under UV-illumination without the nanoparticles were first bearded out to rationalize the photocatalytic activity of the TiO₂ nanoparticles. This, blank experiment result indicated that MO could not be decomposed without the photocatalyst. By contrast introduction of the photocatalysts induced the rapid degradation of MO. Fe-doped TiO₂ nanoparticles gave rise to higher photocatalytic activities than undoped TiO₂. The 7 at% Fe-doped TiO₂ photocatalyst led to the highest degradation rate, i.e. 88.12% after 150 min of UV light irradiation, whereas 0 at% Fe-TiO₂ TiO₂, 1 at% Fe-TiO₂ and 3 at% Fe-TiO₂, 5 at% Fe-TiO₂ samples yielded decomposition rates of 55.6%, 64.3%, 71.5% and 77.9% respectively (**Fig. 13b**).

The photocatalytic mechanism proposed for the Fe-doped a-TiO₂ nanoparticles under visible light is shown in **Fig. 14**. Upon visible illumination, electrons in the VB could be excited to the CB of the oxide, with the concomitant formation of the same quantity of holes in the VB, leading to the formation of an electron–hole pair. Further charge separation and migration of the generated charge carriers towards the surface of catalyst can then lead to redox reactions with organics. The high oxidative potential of the hole (h⁺(VB)) in the catalyst allows direct oxidation of MO to reactive intermediates. Very reactive hydroxyl radicals can also be formed by the decomposition of water.

On the other hand, the reaction of electrons with dissolved oxygen molecules to give superoxide radical anions, $O_2^{\cdot-}$, yielding hydroperoxyl radicals HO_2^{\cdot} on protonation and finally OH^{\cdot} radicals will be more efficient.



As can be seen from **Fig .15**, the photodegradation of MO by Fe-doped TiO_2 nanoparticles followed a first-order rate law, $\ln(C/C_0)$, Where ' C_0 ' is initial concentration of methyl blue (mg/l), ' C ' is the concentration of the dye at various interval times (mg/l), ' t ' is the illumination time (min) and ' k ' is the reaction rate constant.

The stability of $TiO_2: Fe$ at 7% sample was studied after Photodegradation process by SEM, TEM and FT-IR analysis.

SEM and TEM images of $TiO_2: Fe$ at 7% after Photodegradation process of MO revealed that the nanoparticle sizes become larger (~23 and ~25 nm respectively) due to the adsorption of orange methyl on the surface of our photocatalyst (**Fig. 16(a, b)**) while $TiO_2: Fe$ at 7% FT-IR

spectroscopy after Photodegradation process of MO exhibit the following points (**Fig 16(c)**): -C=C- stretching was observed at 1604 cm^{-1} , the -S=O stretching was observed at 1067.5 cm^{-1} , the -C=N stretching was observed at 1313.7 cm^{-1} , -N-H stretching was observed at 3440.1 and 3385 cm^{-1} , the aromatic -C-H stretch was observed at 3080 and 3028 cm^{-1} , -C-H bending was observed at 905 and 768 cm^{-1} , the -CH_3 vibrations was observed at 1433.5 and 1425 cm^{-1} , Fe-O-Ti vibration band appeared at 589 and 427 cm^{-1} [48]. Thus, we confirmed that there is an adsorption of orange methyl on the surface of our synthesized compound (TiO_2 : Fe at 7%).

Conclusion

In summary, undoped and Fe-doped TiO_2 nanoparticles were successfully synthesized by co-precipitation method and characterized by XRD, TEM, SEM, FTIR, thermal analysis, diffuse reflectance UV-visible spectroscopy, photoelectrochemical measurements, Photoluminescence and BET. The results of the different techniques show that the influence of the doping concentration on the structural, textural and optical properties of TiO_2 could be correlated to the change in crystallite size and the doping amount. In fact, the highest Fe-doping (7%) resulted in the smallest size and best crystallinity. Moreover, 7% Fe-doped oxide titanium yielded the smallest band gap. Furthermore, the increase in zinc amount led to a slight rise of the BET specific area. Furthermore, the photocatalytic activities of the doped and undoped TiO_2 nanoparticles were evaluated by studying the photodegradation of MO dye as a model organic pollutant. The best photocatalytic activity was reached with the 7 at% Fe doped TiO_2 sample due to lower crystallite size and improved light harvesting capability.

Acknowledgments

Financial support from Unité de Recherche Electrochimie, Matériaux et Environnement UREME (UR17ES45), Faculté des Sciences de Gabès, Université de Gabès, Cité Erriadh, 6072 Gabès, Tunisie.

References

1. A. lassoued, M.S. lassoued, F. Karolak, S. Garcia-Granda, B. Dkhil, S. Ammar, A. Gadri, J Mater Sci: Mater Electron. 28, **18480** (2017).
2. W. Ben Soltan, M. S. Lassoued, S. Ammar, T. Toupance, J Mater Sci: Mater Electron
3. A. lassoued, M.S. lassoued, B. Dkhil, A. Gadri, S. Ammar, J.mol.struct. 1148, **276** (2017).
4. W. Cun, Z. Jincai, W. Xinming, M. Bixian, S. Guoying, P. Ping'an, F. Jiamo, Appl. Catal. B: Environmental. 39 **269** (2002).
5. R. Bargougui, A. Oueslati, G. Schmerber, C. Ulhaq-Bouillet, S. Colis, F. Hlel, S. Ammar, A. Dinia, J Mater Sci: Mater Electron. 25 **2066** (2014).
6. A. lassoued, M.S. lassoued, B. Dkhil, A. Gadri, S. Ammar, J.mol.struct. 1141, **99** (2017).
7. A. Eshaghi, R. Mozaffarini, M. Pakshir and A. Eshaghi, Ceramics International. 37, **327** (2011).
8. J. Yu, J. C. Yu and X. Zhao, Journal of Sol-Gel Science and Technology 24, **95** (2002).
9. A. Sobhani-Nasab, M. Behpour, J. Mater. Sci. 27, **11946** (2016)
10. M. Grotzel, Nature 414, 338 (2001)
11. Z. Liu, Y. Li, C. Liu, J. Ya, E. Lei, W. Zhao, D. Zhao, L. An, ACS Appl. Mater. Interfaces 3, **1721** (2011).
12. S.S. Kim, J. Jo, C. Chun, J.C. Hong, D.Y. Kim, J. Mater. Chem.16, **370** (2006).
13. C. Damm, F.W. Muller, G. Israel, S. Gablenz, H.P. Abicht, Dyes Pigm. 56, **151** (2003).
14. J. A. Navio, G. Colh, M. I. Litter and G. N. Bianco, Journal of Molecular Catalysis A: Chemical. 106, **267** (1996).
15. K.Maekawa, O. Chiyoda, S. Ohshiro, S.Okada, M. Anpo, H.Yamashita, C. R. Chimie. 9, **817** (2006).
16. M.M. Momeni, Y. Ghayeb, Z. Ghonchehi, Ceramics International. 41, **8735** (2015).
17. M.M. Momeni, Applied Surface Science. 357, 160 (2015).

18. M.M. Momeni, M. Hakimian, A. Kazempou, *Ceramics International*. 41, 13692 (2015).
19. M.M. Momeni, Y.Ghayeb, *Ceramics International*. 42, 7014 (2016).
20. N. Xu, Z. Shi, Y. Fan, J. Dong, J. Shi, C. Hu, *Ind. Eng. Chem. Res.* 38, **373** (1999) .
21. M.M. Momeni, Z. Nazari, *Ceramics International*. 42, 8691 (2016).
22. M.M. Momeni, Y.Ghayeb, *Journal of Alloys and Compounds*. 637, 393 (2015).
23. M.M. Momeni, Y.Ghayeb, M. Davarzadeh, *Journal of Electroanalytical Chemistry*. 739, 149 (2015).
24. L. Davydov, E.P. Reddy, P. France, P.G. Smirniotis, *J. Catal.* 203, **157** (2001).
25. W. Choi, A. Termin, M.R. Hoffmann, *J. Phys. Chem.* 98, **13669** (1994).
26. M.M. Momeni, Y.Ghayeb, *Journal of Electroanalytical Chemistry*. 751, 43 (2015).
27. M.M. Momeni, Y.Ghayeb, F. Ezati, *Journal of Colloid and Interface Science*. 514, 70 (2018).
28. N. Serpone, D. Lawless, J. Didier, J.M. Herrmann, *Langmuir*. 10, **643** (1994).
29. B. Sun, E.P. Reddy, P.G. Smirniotis, *J. Catal.* 237, **314** (2006).
30. K. Bhattacharyya, S. Varma, A.K. Tripathi, A.K. Tyagi, *J. Mater. Res.* 25, **125** (2010).
31. W.Ch. Hung, Y.Ch. Chen, H. Chu and T.K. Tseng, *Applied Surface Science*. 255, **2205** (2008).
32. S. Wang, J.S. Lian, W.T. Zheng and Q. Jiang, *Applied Surface Science*. 263, **260** (2012).
33. J. Tian, H.Gao, H. Kong, P. Yang, W. Zhang and J. Chu, *Nanoscale Research Letters*. 8, **533** (2013).
34. M. Alam Khan, S.Woo and O. B. Yang, *International Journal of Hydrogen Energy*. 33, **5345** (2008).
35. D. H. Kim, H. S. Hong, S. J. Kim, J. S. Song and K. S. Lee, *Journal of Alloys and Compounds*. 375, **259** (2004).

36. L. Wen, B. Liu, X. Zhao, K. Nakata, T. Murakami and A. Fujishima, *International Journal of Photoenergy*. 2012, **1** (2012).
37. B. Liu, X. Wang, G. Cai, L. Wen, Y. Song, X. Zhao, *J. Hazard. Mater.* 169, **1112** (2009).
38. H.P. Klug, L.E. Alexander, *X-ray Diffraction Procedures*, Wiley Interscience Publication, New York, 1974.
39. W.Ch. Hung, Y.Ch. Chen, H. Chu and T.K. Tseng, *Applied Surface Science*. 255, **2205** (2008).
40. P.P. Sahay, R.K. Mishra, S.N. Pandey, S. Jha, M. Shamsuddin, *Curr. Appl. Phys.* 13, **479** (2013).
41. V.D. Binas, K.S. T. Maggos, A. Katsanaki, G. Kiriakidis. *Applied Catalysis B: Environmental*. 113, **79** (2012).
42. Colón G, Maicu M, Hidalgo MC, Navío JA. *Applied Catalysis B: Environmental*. 67, **41** (2006).
43. R. Branek, H. Kisch, *Photochemical and Photobiological Sciences*. 7, **40** (2008).
44. J. I. Pankove, *Optical processes in semiconductors*, Prentice-Hall Inc. Englewood Cliff, New Jersey. **34** (1971).
45. B. Choudhury, A. Choudhury, *J. Lumin.* 132, 178 (2012).
46. C. H. Kim, B. H. Kim and K. S. Yang, *Carbon*. 50, **2472** (2012).
47. K.S.W. Sing, D.H. Everett, R.A.W. Haul, L. Moscou, R.A. Piero-tti, J. Rouquerol, T. Siemieniewska, *Pure Appl. Chem.* 57, **603** (1985).
48. R. Nandini, B. Vishalakshi, *Chem.Eur. J.* 9, **1** (2012).

Table captions

Table 1: (101) Peak position and particule dimension (D)

Table 2: Particule dimension estimated using Scherer Method, and from TEM and SEM data

Table 3: Band gap energy, Energy level of conduction band and valence band of samples with different iron concentrations

Table 4: flat band energy of Fe doped TiO₂ nanoparticles

Figure captions

Fig. 1: The flow chart of prepared undoped and Fe-doped TiO₂ by ultrasound method

Fig. 2: X-ray diffraction spectra (a) and of undoped and XRD peaks corresponding to crystallographic plane (101) (b) of undoped and Fe-doped TiO₂ nanoparticles with different Fe doping contents

Fig. 3: (a) Variation of lattice parameter 'a' and, (b) variation of lattice parameter 'c' for different iron doping concentrations

Fig. 4: TEM images: (a) 0 % Fe–TiO₂, (b) at 1 % Fe–TiO₂, (c) at 3% Fe-TiO₂, (d) at 5% Fe-TiO₂ and (e) 7% Fe-TiO₂ of undoped and doped Fe-TiO₂

Fig. 5: SEM images: (a) 0 % Fe–TiO₂, (b) at 1 % Fe–TiO₂, (c) at 3% Fe-TiO₂, (d) at 5% Fe-TiO₂ and (e) 7% Fe-TiO₂ and a typical EDX spectrum (f).

Fig. 6: Spectra FTIR of TiO₂ in both states: Undoped (a) and 7% Fe-TiO₂ (b)

Fig. 7: TGA and DTA curve of amorphous TiO₂.

Fig.8: Tauc plot (a) of TiO₂ obtained from the chemical precipitation method and Variation of the band gap energy (b) with different concentration.

Fig. 9: Dependence of photovoltage (V versus Ag/AgCl) of Fe doped TiO₂ (Fe = 1, 3, 5, and 7 at. wt.%) on pH of electrolyte.

Fig. 10: Photoconversion efficiency for undoped and doped Fe-TiO₂ (Fe = 1, 3, 5, and 7 at. wt.%)

Fig. 11: Emission fluorescence profile of amorphous and TiO₂: Fe at 7%

Fig. 12: Nitrogen adsorption–desorption isotherms of undoped TiO₂ (a) and TiO₂: Fe at 7% (b) samples.

Fig. 13: Photodegradation kinetics (a) and bar diagram for the % degradation (b) of MO dye in the presence of Fe-doped TiO₂ nanoparticles

Fig. 14: Schematic illustration of the photocatalytic mechanism using Fe doped nanoparticles under visible light.

Fig.15: The pseudo first order kinetics of degradation of Methyl Orange dye over 1 % Fe–TiO₂, at 3 % Fe–TiO₂, at 5% Fe-TiO₂ and 7% Fe-TiO₂ under UV.

Fig.16: TEM and SEM images of 7% Fe-TiO₂ (a, b) and Infrared spectra (c) after Photodegradation process